Erbium incorporation in LiNbO₃ by diffusion-doping

I. Baumann[1], R. Brinkmann[1], M. Dinand[1], W. Sohler[1], L. Beckers[2], Ch. Buchal[2], M. Fleuster[2], H. Holzbrecher[2],
H. Paulus[3], K.-H. Müller[3], Th. Gog[4], G. Materlik[4], O. Witte[5], H. Stolz[5], W. von der Osten[5]

[1] Universität-GH Paderborn, FB6 - Angewandte Physik, Warburger Str. 100, 33098 Paderborn, Germany
(Fax: + 49-5251/603422)
[2] Institut für Schicht- und Ionentechnik ISI, Forschungszentrum Jülich, 52425 Jülich, Germany
(Fax: + 49-2461/614673)
[3] Institut für Technologie- und Wissenstransfer im Kreis Soest, FB Elektrische Energietechnik der Universität-GH Paderborn,
Abt. Soest, Lübecker Ring 2, 59494 Soest, Germany
(Fax: + 49-2921/378266)
[4] Hamburger Synchrotronstrahlungslabor HASYLAB am Deutschen Elektronen-Synchrotron DESY, Notkestr. 85, 22603 Hamburg,
Germany
(Fax: + 49-40/89982787)
[5] Universität-GH Paderborn, FB6 - Experimentalphysik, Warburger Str. 100, 33098 Paderborn
(Fax: + 49-5251/603710)

Abstract. The erbium incorporation into LiNbO₃ by diffusion doping is investigated in detail by means of Secondary Ion Mass Spectrometry, Secondary Neutral Mass Spectrometry, Rutherford Backscattering, Atomic Force Microscopy, X-ray Standing Wave technique and optical site-selective spectroscopy. The diffusion of erbium in LiNbO₃ can be described by Fick's laws of diffusion with a concentration-independent diffusion coefficient. The diffusion constants and activation energies for Z-cut (X-cut) LiNbO₃ are 4.8×10^{-5} cm²/s (12.0×10^{-5} cm²/s) and 2.28 eV (2.44 eV), respectively. A limited solubility of erbium in LiNbO₃ has to be taken into account increasing exponentially with rising temperature. During the first step of diffusion an $Er_x Nb_y$-oxide layer is formed at the surface of the sample acting as diffusion reservoir. Erbium is incorporated into LiNbO₃ on vacant Li-sites slightly shifted from the original Li-position along the (-c)-direction. Site-selective spectroscopy found four distinguishable energetically different erbium centres at this lattice site resulting from locally different symmetries of the crystal field.

Lithium niobate (LiNbO₃) is one of the most attractive materials for integrated optics due to its combination of excellent electrooptical, acoustooptical and non-linear optical properties. The lithium deficit of LiNbO₃ of congruent composition (Li/Nb = 0.94) [1, 2, 3] enables due to the resulting point defect structure [4, 5] the incorporation of dopants up to several mole% on regular lattice sites [6, 7, 8, 9]. Integrated optical amplifiers and lasers can be realised by doping a LiNbO₃ substrate with rare earth ions (Er, Nd, Yb, Tm) [10, 11, 12, 13, 14, 15]. In particular, erbium-doped devices are of great interest for applications in optical communication in the wavelength range around $\lambda = 1.55$ μm. Travelling wave amplifiers [16], different types of lasers (fixed frequency Fabry-Perot-type lasers with dielectric mirrors [17], modelocked laser [18], tuneable laser [19] and DBR-laser [20]) as well as loss-compensated optical spectrum analysers and filters in Er:LiNbO₃ [21, 22] have already been demonstrated.

Several doping techniques have been investigated during the last few years to prepare Er:LiNbO₃. Besides doping of the bulk during crystal growth, ion implantation [23], pulsed laser deposition (PLD) [24] and indiffusion of an erbium layer [10] have been studied. The latter three techniques allow the use of commercially available LiNbO₃ wafers of excellent quality and the local doping of selected parts of the wafer surface. This is important for the integration of active and passive devices on the same chip due to the three-level character of the transitions around $\lambda = 1.5$ μm [25]. Erbium diffusion doping proved to be the simplest and most efficient technique yielding highly doped surface regions of excellent quality. After the erbium diffusion doping low-loss optical channel waveguides can be defined using the well established technique of titanium indiffusion. The knowledge of the diffusion constants and the solubility of erbium is necessary for the fabrication of low-loss Ti:Er:LiNbO₃ waveguides with optimised overlap of doping profile and intensity distribution of the guided modes. The lattice sites occupied by the

* *Present address:* ALCATEL, Abt. BFN/MT, Löffelholzstr. 20, 90441 Nürnberg
(Fax: + 49-911/4230485, E-mail: I.Baumann@ nbg.sel.alcatel.de)

erbium ions give information about the incorporation mechanism.

In this paper we summarise the results of our investigations of the incorporation of erbium into $LiNbO_3$ by diffusion doping. The diffusion constants and the maximum solubility of erbium in $LiNbO_3$ were determined by analysing erbium doping profiles using SIMS (Secondary Ion Mass Spectrometry) and SNMS (Secondary Neutral Mass Spectrometry). The evolution of the formation of a surface compound due to chemical reactions between deposited erbium layer and the $LiNbO_3$ substrate was studied by RBS (Rutherford Backscattering) and SNMS. The surface morphology influenced by the formed surface compound was investigated by AFM (Atomic Force Microscopy). The geometric lattice site of erbium in $LiNbO_3$ was determined using the X-ray Standing Wave technique (XSW). Absorption spectroscopy as well as site-selective luminescence spectroscopy was used to investigate the local energetical environment of erbium.

1 Experimental

1.1 Sample Preparation

$LiNbO_3$ wafers grown from a congruent melt produced commercially by Crystal Technology Inc. were used for diffusion doping.

For the determination of the diffusion constants and the solubility of erbium in $LiNbO_3$ X-cut and Z-cut samples were prepared. Erbium was deposited on the surface of the sample by electron beam evaporation at 8×10^{-5} Pa. One set of samples was covered with 18.0 nm metallic erbium, a second one with 22.3 nm Er_2O_3 fabricated by in-situ oxidation of erbium during evaporation in an oxygen atmosphere $(p_{O_2} = 4 \times 10^{-2}$ Pa$)$. In both cases this results in an erbium surface coverage of $(6.0 \pm 0.2) \times 10^{16}$ cm^{-2} determined by RBS. This figure is consistent with results of calculations assuming the corresponding bulk densities for the deposited layers. Metallic erbium is usually used for planar doping. However, photolithographical structuring of metallic erbium layers for local doping is not possible due to chemical reactions in slightly acid solutions (pH ≤ 7), leading to the formation of water soluble erbium compounds. Er_2O_3 layers are more stable and therefore allow local doping by applying photolithography.

The diffusion was carried out in a platinum box over 30 hours at temperatures of 920 °C, 960 °C, 1010 °C, 1060 °C, 1100 °C and 1130 °C, respectively, within the high temperature stability range of the ferroelectric phase of congruent $LiNbO_3$ (900 °C–1142 °C) [26]. During the first two hours the diffusion was performed in a dry oxygen atmosphere to fully oxidise the erbium layer followed by a diffusion in argon atmosphere. The last hour of diffusion was carried out in oxygen atmosphere to compensate losses of oxygen of the crystal during the diffusion and to obtain a complete oxidation of the samples.

An additional set of X-cut samples was prepared to investigate the surface morphology in dependence of the erbium surface concentration and of the depletion of the diffusion reservoir. The fabrication parameters are summarised in Table 1. The diffusion data obtained from the samples mentioned above were used to prepare samples with known different degrees of depletion of the diffusion reservoir. For the samples of the first column of the table this results in an undepleted diffusion reservoir. This is just exhausted for the samples of the second column. The diffusion reservoir of the samples of the third column is completely depleted and the erbium depth profile is nearly Gaussian.

For the XSW-measurements a nearly perfect crystal with a surface of high quality is needed to allow the formation of a standing wave pattern. To obtain a diffusion-doped $LiNbO_3$ substrate with low strain an erbium layer of only 2.3 nm thickness was diffused at 1060 °C/40 h resulting in an erbium surface concentration of 3.2×10^{19} cm^{-3}.

For the spectroscopic investigations, by way of exception, a bulk-doped X-cut $Er:LiNbO_3$ sample of congruent composition was used with geometric dimensions of $(10 \times 6 \times 1)$ mm^3 grown by *Wang Lianfeng at Tianjin University, China.* The erbium concentration was $C_{Er} = 3.71 \times 10^{19}$ cm^{-3}.

1.2 Analytical techniques

To analyse the concentration profile of the indiffused erbium quantitatively with high accuracy SIMS as well as SNMS [27, 28] were used.

SIMS measurements were performed with a CAMECA-IMS4F instrument. An O_2^+-beam of 300 nA at 5.5 keV was used to sputter a crater of 200×200 μm^2 cross section with a rate of about 0.6 nm/s. The yields of $^{93}Nb^+$ and $^{166}Er^+$ were recorded as function of time. Only ions from a central area of 8 μm diameter inside the crater were detected. To provide good surface conductivity needed for sputter profiling 50 nm gold was deposited on the surface of the $LiNbO_3$ sample. During sputtering the sample was continuously flooded with electrons to avoid uncontrolled charging. The detection sensitivity of erbium in $LiNbO_3$ using SIMS was 2 ppm.

SNMS measurements were performed with the High Frequency Mode (HFM) [29, 30] of electron gas SNMS on a Specs INA-3 [31]. To avoid charging effects during depth profile analysis of insulating materials a high-frequency rectangular shaped voltage is applied to the sample. During the negative part of the HF-cycle the sample is sputtered by the extracted positive plasma ions and a positive charge on the surface is accumulated. This charge is compensated when the accelerating voltage is switched off and the positive charged surface attracts

Table 1. Fabrication parameters of the samples for the investigation of the surface morphology. Diffusion time $t_{diff} = 30$ h. T_{diff} - diffusion temperature, d_{Er} - deposited erbium layer thickness

$T_{diff}/°C$	d_{Er}/nm		
1060	12.2	3.9	3.1
1100	12.2	7.2	3.9
1130	12.2	11.3	7.2

electrons from the plasma towards the sample. An acceleration voltage of 700 V at a frequency of 430 kHz was chosen to optimise the sputter yield. Crater effects were minimised by covering the targets with a Cu-mask with a 3 mm aperture. With a total sputter yield of 0.3 atoms/ion a sputter rate of about 0.8 nm/s was achieved. The detection sensitivity of erbium in LiNbO$_3$ using SNMS was 40 ppm.

The disadvantage of SNMS compared with SIMS is a lower signal to noise ratio leading to a lower sensitivity. But SNMS decouples the sputtering and ionisation processes. Therefore, the atom-to-ion conversion efficiency is essentially a constant of the apparatus and chemical matrix effects as known for SIMS are practically absent in this method. SNMS was used to confirm the results of the SIMS measurements for high erbium concentrations and to reveal changes of the chemical composition at the surface of the LiNbO$_3$ substrate.

The measured erbium profiles were normalised to the niobium signal. The quantitative determination of the erbium concentration was possible by analysing a melt doped standard crystal containing 0.19 wt% Er$_2$O$_3$ in LiNbO$_3$ corresponding to 2.77×10^{19} cm^{-3}. The depth of the craters was measured by a depth profiler (DEKTAK) and a linear time versus depth relationship was assumed.

For an independent confirmation of the erbium distribution near the surface and of the formation of a surface compound RBS was used [32]. RBS experiments were performed with He^{++} ions. The ion energy was 4.5 MeV. Energy and rate of the 170° backscattered helium ions were detected by a silicon detector (FHWM 13 keV). The obtained depth resolution was about 25 nm.

The surface morphology of the doped samples was investigated by an atomic force microscope (TMX 2000 Explorer from Topometrix). The contact mode was used to get a high vertical and lateral resolution.

XSW experiments to determine the lattice site of erbium in LiNbO$_3$ were performed at the RÖMO I station of the Hamburger Synchrotronstrahlungslabor Hasylab. The method is described in detail in [33, 34, 35]. The experimental set-up is sketched in the insets of Fig. 8. When a plane wave of X-rays is diffracted in a perfect crystal by a set of (hkl) diffraction planes, incident and diffracted beam interfere to form a standing wave field which has the periodicity of the lattice planes. It shifts into the crystal by an amount of half a planar spacing if the incident angle of the X-rays is advanced towards higher angles through the Bragg reflection. Atoms located within the maximum intensity of the standing wave field will be excited. Secondary yields such as fluorescence from impurity atoms will be modulated accordingly. By comparing the phase of the measured signal with the known phase of the standing wave field with respect to the diffraction planes, the relative position of the impurity within the planar spacing is revealed.

To investigate the energetic structure of erbium in the LiNbO$_3$ host absorption and site-selective spectroscopy were applied. Both absorption and luminescence spectra were measured in π- and σ-polarisation i.e. $\vec{k} \perp \vec{E}$, $\vec{k} \parallel c$ and $\vec{k} \perp \vec{E}$, $\vec{k} \perp c$, respectively, where $\vec{k}$ is the light wave vector, $\vec{E}$ is the electric field vector and c denotes the optical axis of the crystal. The absorption experiments in the energy range of 1.87–3.28 eV were carried out using a halogen lamp. Site-selective excitation of luminescence spectra were obtained using a dye laser (1.53–1.57 eV, Styrol 8, and 1.838–2.018 eV, DCM, respectively) pumped by an argon ion laser. The laser line was accurate in position to 0.05 meV and had a spectral width of 0.15 meV. All spectra were recorded with a monochromator SPEX 1403. The measurements were done at 5 K with the sample mounted in a helium flow cryostat.

2 Experimental results and discussion

2.1 Erbium indiffusion

2.1.1 Determination of the diffusion data-diffusion constants, activation energy and solubility. To determine diffusion data from depth profiling an adequate description of the character of the diffusion is necessary. Considering the diffusion data of different metallic dopants in LiNbO$_3$ [36] a general description of the diffusion by Fick's laws seems to be allowed. For dilute solutions as in our case the diffusion coefficient, a second rank tensor, can be taken as constant. Therefore, a concentration-independent diffusion coefficient, D_{Er}, will be assumed for the description of the planar erbium diffusion in LiNbO$_3$.

The mathematical theory of diffusion is based on the hypothesis that the current density of diffusing matter $\vec{j}_c$ is proportional to the concentration gradient $\vec{\nabla} c$. This can be written as:

$$\vec{j}_c = - D (\vec{\nabla} c) \tag{1}$$

In combination with the equation of continuity

$$\frac{\partial c}{\partial t} + \vec{\nabla} \cdot \vec{j}_c = 0 \tag{2}$$

the general diffusion equation can be expressed as

$$\frac{\partial c}{\partial t} = \vec{\nabla} \cdot [D (\vec{\nabla} c)]. \tag{3}$$

Using planar doping the erbium concentration profiles can be derived from the one-dimensional diffusion equation corresponding to Fick's law

$$\frac{\partial c_{Er}(y,t)}{\partial t} = D_{Er} \frac{\partial^2 c_{Er}(y,t)}{\partial y^2}, \tag{4}$$

where y is the direction normal to the substrate surface and c_{Er} is the erbium concentration. Taking into account a finite solid solubility of erbium in LiNbO$_3$ the erbium concentration at the surface of the substrate is constant as long as the erbium reservoir is not depleted. The corresponding solution of equation (4) is a complementary error function:

$$c_{Er}(y,t) = c_{Er,0} \operatorname{erfc} \left(\frac{y}{2\sqrt{D_{Er}t}} \right) \quad (t \leq t_1), \tag{5}$$

where $c_{Er,0}$ is the surface concentration of erbium and corresponds to the temperature dependent solid solubility of erbium in LiNbO$_3$ and $2\sqrt{D_{Er}t}$ is the diffusion depth [37]. At the time $t = t_1$, which can be evaluated from the

law of mass conservation, the reservoir is depleted. For $t > t_1$ the solution can be written as [38]

$$c_{Er}(y,t) = \frac{c_{Er,0}}{2\sqrt{\pi D_{Er} t}} \int\limits_0^{+\infty} \left[\text{erfc}\left(\frac{y'}{2\sqrt{D_{Er} t_1}} \right) \right] (g(y,y',t) \mathrm{d}y' \tag{6}$$

$$g(y,y',t) = \exp\left[-\left(\frac{y'+y}{2\sqrt{D_{Er}(t-t_1)}} \right)^2 \right] + \exp\left[-\left(\frac{y'-y}{2\sqrt{D_{Er}(t-t_1)}} \right)^2 \right].$$

For $t \gg t_1$ the solution can be approximated by the Gaussian function

$$c_{Er}(y,t) = \tilde{c}_{Er}(t) \exp\left[-\left(\frac{y}{2\sqrt{D_{Er} t}} \right)^2 \right] \tag{7}$$

with an erbium surface concentration

$$\tilde{c}_{Er}(t) = \frac{\rho_{Er} d_{Er} N_A}{M_{Er,rel} \sqrt{\pi D_{Er} t}} \leq c_{Er,0}$$

resulting from the law of mass conservation

$$\frac{\rho_{Er} d_{Er} N_A}{M_{Er,rel}} = \int\limits_0^\infty c_{Er}(y,t) \mathrm{d}y, \tag{8}$$

where ρ_{Er} is the density of the evaporated erbium layer, d_{Er} the thickness of the deposited erbium layer and N_A the Avogadro constant and $M_{Er,rel}$ the relative mass of erbium.

The unambiguous determination of the diffusion coefficients *and* the solubility is only possible by erbium concentration profiles corresponding to equation (5). Therefore, a suitable set of samples was prepared by diffusion doping as described above resulting in undepleted diffusion reservoirs at the surface. Some of the erbium concentration profiles measured by SIMS and SNMS are shown in Fig. 1.

Erbium rich surface compounds of about 150–250 nm thickness were observed on the surface; they represent the undepleted diffusion reservoirs. The subsequent erbium doping profile suggests an erbium distribution corresponding to Eq. (5). The transitions between the erbium-rich surface compounds and the concentration profiles correspond to the maximum solubilities $c_{Er,0}$ of erbium in LiNbO$_3$ at the different diffusion temperatures.

Least square fits of complementary error functions corresponding to Eq. (5) give a good agreement with the measured doping profiles below the surface compound, shown as an example for the SNMS results as dash-dotted line. The parameters of the fits yield the diffusion coefficients and the solubility data. The main uncertainty of these data results from the limited accuracy of the depth scaling. In particular, the determination of the layer thickness of the surface compound was difficult due to the roughness of the undepleted surface (see also the following chapter). An uncertainty of about 100 nm remains in the scaling of the depth, resulting in an accuracy of the diffusion coefficients of about $\pm 7 \times 10^{-16}$ cm^2/s and

		cut	T_{diff} (°C)
a	SIMS	x	1060
b	"	z	1060
c	"	x	1100
d	SNMS	x	1130
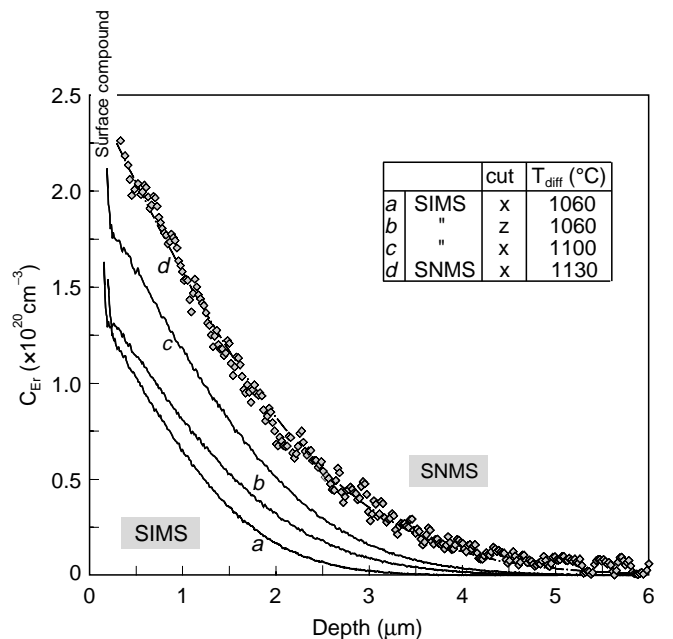
Fig. 1. Typical erbium doping profiles obtained by SIMS and SNMS for different crystal orientations and different diffusion temperatures (1060 °C $\leq T_{diff} \leq$ 1130 °C). The dash-dotted line reveals the fit corresponding to Eq. (5) for the SNMS erbium depth profile. Due to the chosen experimental diffusion conditions the erbium diffusion reservoir at the surface is not completely depleted. A thin surface compound consisting of erbium-niobium-oxide of about 150–250 nm remains at the surface

$\pm 1 \times 10^{-14}$ cm^2/s for the 920 °C and 1130 °C diffusion, respectively.

The Arrhenius plot in Fig. 2 summarises all diffusion coefficients obtained from the analysis of the measured erbium profiles. No difference in the diffusion was found using metallic erbium or erbium oxide deposition on the LiNbO$_3$ surface. Both SIMS as well as SNMS measurement results fit well with

$$D_{Er} = D_{Er,0} \exp\left(-\frac{E_a}{k_B T} \right), \tag{9}$$

where k_B is Boltzmann's constant and T is the diffusion temperature, shown by the dash-dotted lines in Fig. 2. The diffusion constants $D_{Er,0}$ and activation energies for diffusion E_a given in Table 2 were determined by the fit to the SIMS results only due to the higher sensitivity of this method in comparison with SNMS. The erbium diffusion data published earlier [10] are within the given accuracy in agreement with those given above.

The measured erbium profiles (a) and (b) in Fig. 1 indicate that the solubility of erbium in LiNbO$_3$ shows no anisotropic behaviour; it is presented in Fig. 3 as function of temperature. Comparing this presentation with the phase diagrams of TiO$_2$-LiNbO$_3$ [6] and Fe$_2$O$_3$-LiNbO$_3$ [7] it can be concluded that the line fitted to the measured solubility data presents a phase boundary between a solid solution of Er:LiNbO$_3$ (shaded area) and different co-existing phases towards higher erbium concentrations. Therefore, Fig. 3 can be considered as a small part of the
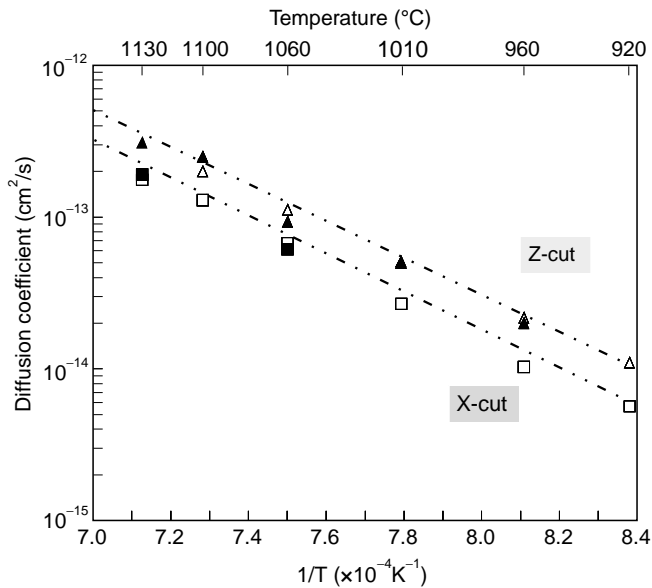
Fig. 2. Arrhenius plot of the diffusion coefficients of erbium in LiNbO$_3$ for diffusion parallel to the *c*-axis - Z-cut - (*triangle*) and perpendicular to the c-axis - X-cut - (*squares*) of the LiNbO$_3$ crystal obtained by SIMS (white) and SNMS (black). The *dash-dotted lines* corresponds to Eq. (10)

Table 2. Diffusion constants and activation energies for erbium diffusion in LiNbO$_3$

	$D_{Er,0}/ \times 10^{-5}$ cm^2/s	E_a/eV
Diffusion $\parallel c$ (Z-cut)	4.8 ± 0.5	2.28 ± 0.04
Diffusion $\perp c$ (X-cut)	12.0 ± 2.0	2.44 ± 0.04

pseudobinary phase diagram LiNbO$_3$-Er$_2$O$_3$. A detailed compositional phase analysis is necessary to describe the phases which are in equilibrium for higher erbium concentrations (for example Er : LiNbO$_3$, Er$_3$NbO$_7$, ErNbO$_4$, ..).

In systems of very limited solubility an exponential law describes the rise of the solubility with the temperature:

$$c_{Er,0} = c_s \exp\left(-\frac{\Delta H_s}{k_B T} \right), \qquad (10)$$

where ΔH_s is the heat of solution and c_s is the solubility constant [39]. The Arrhenius plot of the solubility data shown in the inset in Fig. 3 fits well with equation (10). $\Delta H_s = 1.36$ eV and $c_s = (1.8 \pm 0.3) \times 10^{25}$ cm^{-3} were found, respectively.

Photoluminescence measurements of erbium implanted in LiNbO$_3$ showed that the amount of optically active erbium in LiNbO$_3$ incorporated at 1060 °C is limited to 0.18 at % [40]. This observation suggests that the solubility limit coincides with the amount of optically active erbium in LiNbO$_3$.

The determined diffusion data of erbium in LiNbO$_3$ confirm the assumption of a diffusion corresponding to Fick's laws. A limited solubility of erbium in LiNbO$_3$ must be taken into account. The validity of this result will be underlined by the comparison of the measured and the calculated evolution of an erbium concentration profile in Z-cut LiNbO$_3$ (13.2 nm Er, 1100 °C/100 h) during diffusion with parameters as used for the fabrication of Ti : Er : LiNbO$_3$ amplifiers [16] (see Fig. 4.) After 30 h of diffusion the erbium reservoir is not yet depleted and the concentration profile corresponds to a complementary error function. The concentration profile evolves towards
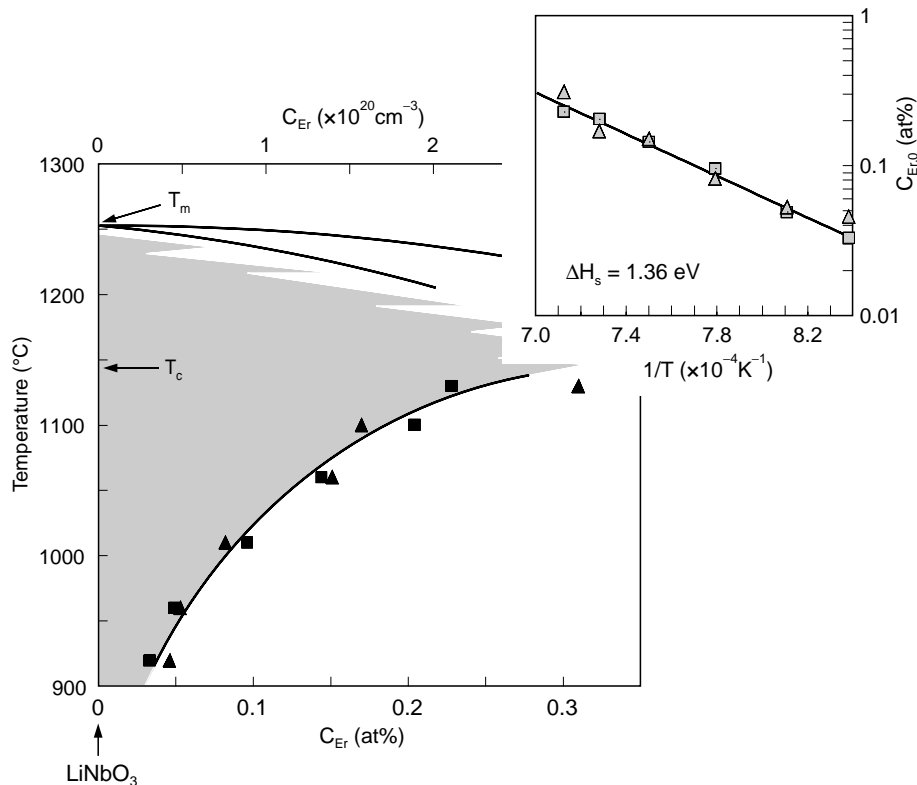
Fig. 3. Erbium solubility in LiNbO$_3$; Solid solubility range of erbium in LiNbO$_3$ in the pseudobinary phase diagram of LiNbO$_3$ - Er$_2$O$_3$ for small erbium concentrations (*shaded area*). (T_m and T_c are the melt temperature and the ferroelectric Curie temperature of pure congruent LiNbO$_3$, respectively; 1 at % = 9.242×10^{20} cm^{-3}).
Inset: Arrhenius plot of the solubility data of erbium in LiNbO$_3$ reveals the exponential increase of the solubility with rising temperature. (ΔH_s - heat of solution)
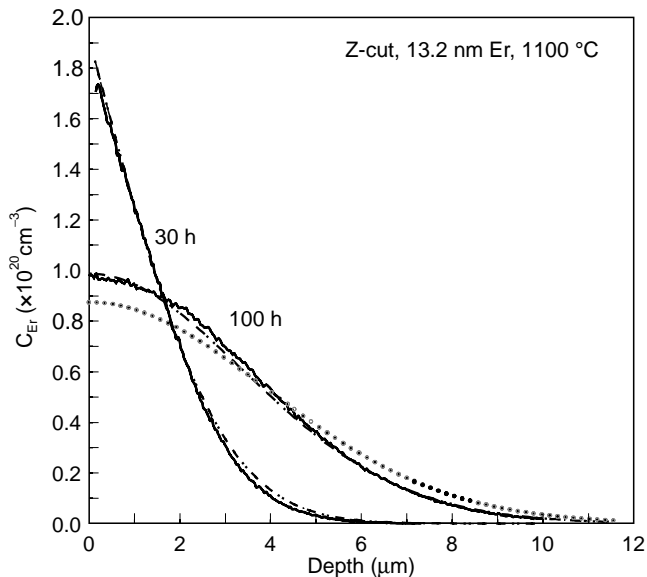
Fig. 4. Evolution of the erbium concentration profile in LiNbO$_3$ during diffusion (Z-cut LiNbO$_3$, $T_{diff} = 1100\,^{\circ}$C, 13.2 nm Er). As long as the diffusion reservoir is not exhausted the erbium profile corresponds to Eq. (5). After consuming the erbium reservoir the erbium profile shift to a Gaussian course corresponding to Eq. (6). The thin dash-dotted lines mark the calculated diffusion profiles. The dotted line presents the calculation resulting from an assumed pure Gaussian diffusion over 100 h without limited solubility

a Gaussian when the diffusion reservoir is exhausted (see diffusion after 100 h). The thin dashed-dotted lines in Fig. 4 reveal the calculated diffusion profiles corresponding to Eq. (5) and Eq. (6). The dotted line presents the calculated erbium doping profile for $1100\,^{\circ}$C/100 h if a pure Gaussian description of the diffusion without limited solubility is assumed. The comparison with the measured depth profile shows that this description is not suitable for the given diffusion parameters.

2.1.2 Erbium-rich surface layer and surface morphology. To characterise the formation of the erbium diffusion reservoir and the surface morphology RBS, SNMS and AFM measurements were performed, respectively.

RBS was used to study the formation and depletion of the erbium-rich compound acting as diffusion reservoir on the surface. The random RBS-spectra shown in Fig. 5 result from the investigation of a X-Cut LiNbO$_3$ sample for a diffusion at $1060\,^{\circ}$C for 1 h, 40 h and 80 h diffusion time, respectively. The solid line (a) corresponds to the deposited erbium film of 13.0 nm on LiNbO$_3$. The niobium signal (at channel 815) is shifted to lower energies due to the coverage with erbium. During heating in an oxygen atmosphere the erbium oxidises completely. The spectrum changes after one hour annealing - see line (b): the erbium peak is broadened significantly and the niobium is diffused into the erbium oxide layer shown by the niobium signal shifted to channel 820. This suggests the formation of an Er$_x$Nb$_y$-oxide layer containing a high concentration of erbium. The erbium to niobium ratio was estimated to be 3:7. This layer of about 80 nm thickness serves as the initial source for erbium diffusion into
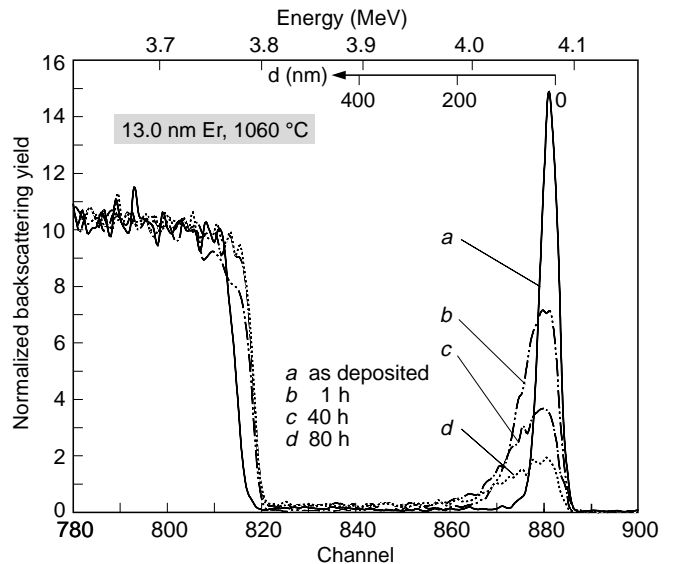

Fig. 5. Steps of erbium indiffusion investigated by RBS using random spectra. The change of the erbium and niobium content with depth is shown. Due to the fast movement of niobium into the erbium oxide layer in the first time of diffusion (at channel 815 and channel 820) the formation of an erbium-niobium-oxide, Er$_x$Nb$_y$-oxide, can be assumed. (Sample: Z-cut, 13.0 nm erbium, annealing at $1060\,^{\circ}$C, t_{diff}: *a*) - as deposited, *b*) 1 h, *c*) 40 h, *d*) 80 h)

the bulk. Its thickness increases with diffusion time (about 115 nm after 80 h). Simultaneously, the layer continuously loses erbium. The small bulk erbium signal at channel 860 and below is determined by the solubility of erbium in LiNbO$_3$.

Using SNMS the compositional changes between the erbium-rich compound on the surface and the bulk substrate was studied. The results of surface-near depth profiling of erbium, lithium and niobium by SNMS after a diffusion at $1130\,^{\circ}$C, shown in Fig. 6, confirmed the RBS observations. For this SNMS-experiment a sample covered with 20.9 nm erbium was heated up to the diffusion temperature of $1130\,^{\circ}$C in a dry oxygen atmosphere, which took 1.75 h. Afterwards, the sample was cooled down.

The oxygen signal, simultaneously measured but not shown in the figure, was constant. It indicates a fully oxidised state of the sample and the formation of an oxide at the surface. Both lithium and niobium move simultaneously into the surface layer as erbium moves into the bulk. The erbium-rich surface compound shows a niobium content comparable to the bulk forming an Er$_x$Nb$_y$-oxide layer of about 210 nm thickness. The erbium concentration near the top of the layer is about 7 at %. The lithium concentration in the erbium-rich surface layer is reduced compared to the bulk as shown by the strong decrease of the lithium signal near the surface. Up to a depth of 1 μm the lithium concentration is reduced due to outdiffusion.

It can be assumed that the initial steps of erbium incorporation into LiNbO$_3$ include the formation of an Er$_x$Nb$_y$-oxide similar to the observations of titanium indiffusion into LiNbO$_3$ investigated by *Armenise* et al. [41] and *Rice and Holmes* [42]. They found that a (Ti$_{0.35}$Nb$_{0.65}$)O$_2$ compound and
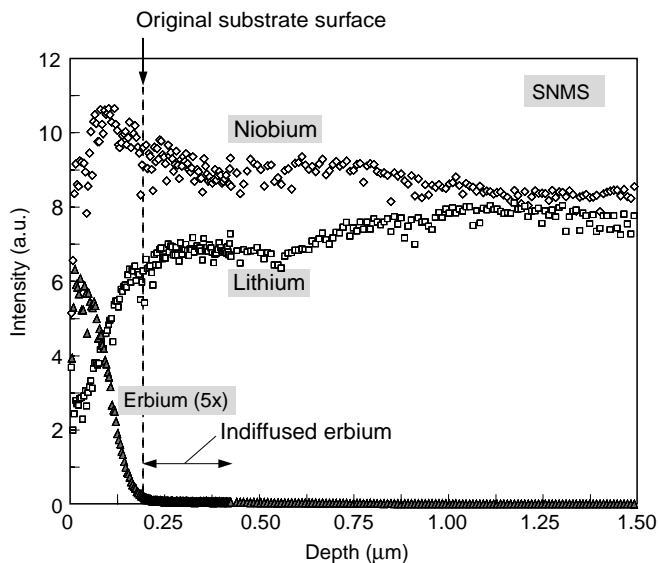
Fig. 6. Formation of the erbium rich compound on top of the substrate during the first step of diffusion studied by SNMS. Niobium enters due to counterdiffusion the erbium layer during heating up and reaches the surface forming an Er_xNb_y-oxide compound on the surface. (Sample: Z-cut, 20.9 nm erbium, heated up to 1130 °C in 1.75 h, afterwards cooling)

a $[(Li_{0.25}Nb_{0.75}O_2)_{0.42}(TiO_2)_{0.58}]$ compound is formed in the early stage of diffusion, respectively. They described the partial formation and the occurrence of $LiNb_3O_8$, respectively. This phase should not appear in our experiments due to the high diffusion temperatures; at $T_{diff} \geq 900$ °C this compound is not stable from the thermodynamic point of view [26]. A consideration about coexisting phases in the Er_xNb_y-oxide compound at the surface, their mixing and their stoichiometry demands a deeper analysis.

To allow the fabrication of low-loss $Ti:Er:LiNbO_3$ waveguides a smooth surface of the substrate is required after diffusion doping. The surface morphology of $Er:LiNbO_3$ depends on the depletion of the diffusion reservoir; this was investigated by AFM as shown in Fig. 7. The surface morphology of undepleted diffusion reservoirs is presented in Fig. 7a–c. Here 12.2 nm erbium were deposited on Z-cut $LiNbO_3$ and diffusion was performed at temperatures 1060 °C $\leq T_{diff} \leq 1130$ °C (see Table 1). The remaining Er_xNb_y-oxide does not form a closed uniform surface coverage. It consists of islands of nearly equal size. The density and height of the islands decrease with T_{diff} and degree of depletion, respectively. This grain-shaped coverage certainly influences the results of the SNMS depth profiling near the surface as shown in Fig. 6. The islands of the Er_xNb_y-oxide determine the roughness of the surface morphology which reduces the depth resolution of each element during depth profiling.

At a diffusion time $t \approx t_1$ (see Eq. (6)) the Er_xNb_y-oxide layer vanishes and the erbium distribution in the bulk is further described by a diffusion profile corresponding to Eq. (6). Fig. 7d shows an example of the resulting surface morphology (11.3 nm erbium diffused at 1130 °C/30 h). No surface roughness was detectable. When the diffusion

reservoir is completely exhausted the surface morphology is comparable to the smooth surface of a virgin substrate.

Due to the low erbium diffusivity compared with the titanium diffusivity the erbium diffusion is performed at higher temperatures than the titanium diffusion for waveguide preparation (1030 °C $\leq T_{diff}(Ti) \leq 1060$ °C). As shown above the solubility of erbium depends on the temperature. Depending on the choice of the diffusion temperature for titanium, $T_{diff}(Ti)$, the erbium surface concentration may be higher than the solubility at this temperature. In that case the surface-near region can be considered as a supersaturated solution and generally the formation of precipitates at the surface can occur. To test this assumption, we additionally annealed our samples prepared at $T_{diff}(Er) \geq 1100$ °C in a second step at 1060 °C/7 h. If the surface reservoir was already depleted independent from the real surface concentration of erbium no change of the surface morphology was detectable. In case of the undepleted surface no further indiffusion from the remained diffusion reservoir was observed. The density of the islands remained constant but their height increased. This means erbium segregation will occur at the surface from the supersaturated solution if some seeds, e.g. remaining Er_xNb_y-oxide islands, exist. To get a smooth, undamaged surface of $Er:LiNbO_3$ for further preparation of waveguides the erbium diffusion reservoir must be completely exhausted.

The results discussed above enable a good qualitative and quantitative description of the erbium indiffusion into $LiNbO_3$ using Fick's laws. In the investigated erbium concentration range the diffusion coefficient of erbium is concentration independent. The solubility of erbium is limited. As long as the diffusion reservoir is not exhausted the surface of the substrate is rough due to island formation of an Er_xNb_y-oxide which forms the diffusion reservoir at high temperatures..

The determination of the lattice site of erbium in $LiNbO_3$ will be described in the following chapter.

2.2 Lattice site of erbium in LiNbO₃

The lattice site of Er^{3+} in $LiNbO_3$, its geometric position and its energetic structure have been studied combining X-ray Standing Wave technique (XSW) and optical spectroscopy.

2.2.1 Geometric lattice site of erbium determined by XSW. Using XSW the complete three-dimensional determination of the erbium position is based on the $(0\,0\,0\,\bar{6})$ reflection and three reflections $(0\,1\,\bar{1}\,4)$, $(1\,\bar{1}\,0\,4)$ and $(\bar{1}\,0\,1\,4)$ belonging to a form connected by rotations of $120°$ around the c-axis of the crystal. This set of reflections is well suited for the geometric lattice site determination since both niobium and lithium ions as well as the structural vacancy of the $LiNbO_3$ crystal structure form single atomic sheets with respect to the corresponding diffraction planes [43].

Measured XSW-data for the reflectivity, Nb- and Er-fluorescence together with theoretical, fitted curves are shown in Fig. 8 for the $(1\,\bar{1}\,0\,4)$ and $(0\,0\,0\,\bar{6})$ reflections, respectively. A summary of the coherent positions, $\Phi_c^{(hkl)}$,

the relative position of the site within the planar spacing of the diffraction planes, and the coherent fractions, $f_c^{(hkl)}$, the percentage of ions occupying this site, extracted from the fits to the experimental results is given in Table 3. The results can be interpreted in terms of an undistorted host lattice and single-site occupancy for erbium atoms. The
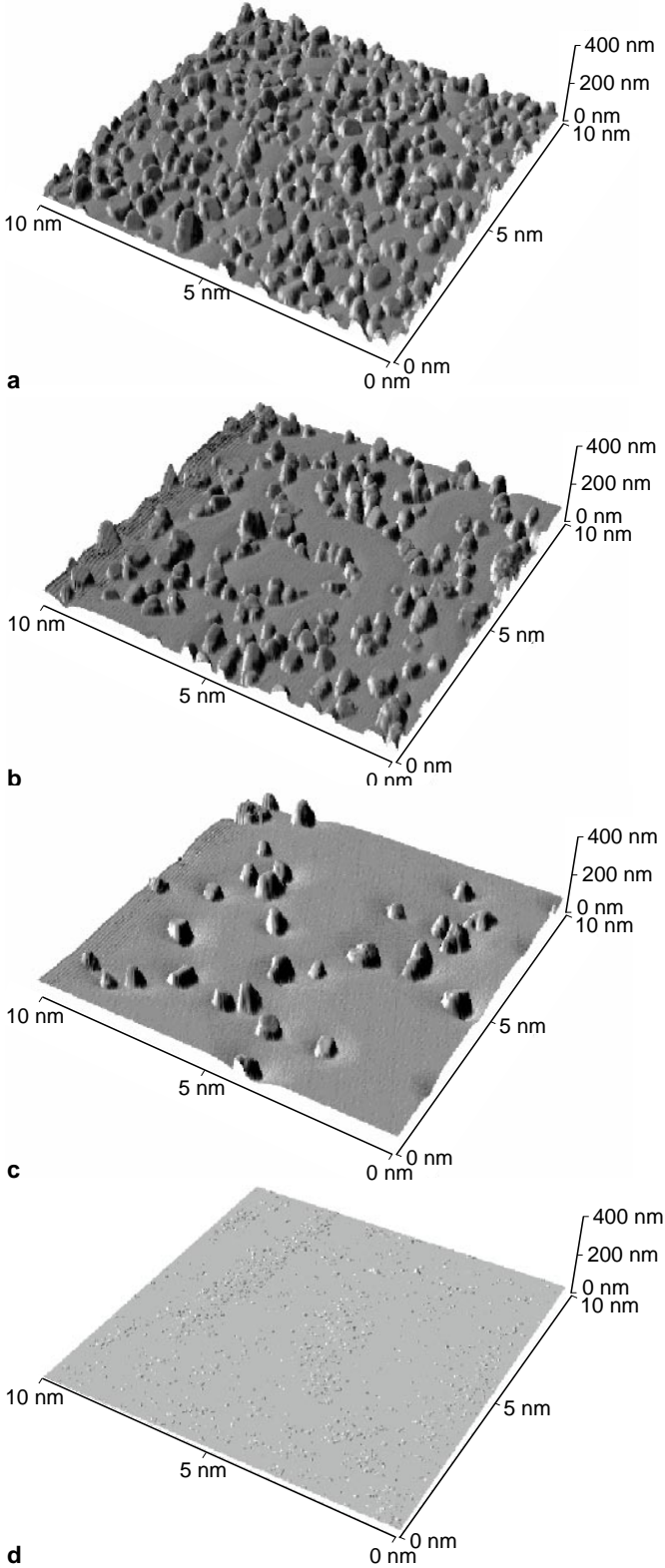
measurements utilising the $\{1\bar{1}0\bar{4}\}$ reflections yielded identical fluorescence signals for both Nb- and Er-ions confirming a three-fold rotational symmetry as expected for the c-axis of the $LiNbO_3$ crystal. As a consequence, this leads to the restriction of possible erbium sites to highly symmetric locations, to stacks formed by Nb- and Li-atoms parallel to the c-axis of the crystal. The measured position places erbium either close to the Li-site or near to the Nb-site.

The ambiguity can be resolved using the $(000\bar{6})$ measurement. The measured coherent position was in good agreement with an erbium ion close to the lithium site and clearly disagreed with a niobium site. Thus, for single-site occupation only the lithium site is left as the one position for the erbium atoms simultaneously consistent with all four standing wave measurements performed. The exact position of erbium is a vacant lithium site with a shift of 0.46 Å parallel to the (-c)-direction (see Fig. 9). Using the Schönfliess notation the site symmetry can be described by C_3 [34].

Considering the coherent fraction of the erbium ions the measurement of the $(1\bar{1}0\bar{4})$ reflection results in higher values than the measurement using $(000\bar{6})$. This effect has been also observed in other $LiNbO_3$ samples doped with Ti and Fe [35]. It strongly suggests that the dopants do not occupy just a single site but obey a distribution function which is extended in the c-direction so that its smaller projection upon the $(1\bar{1}0\bar{4})$ direction leads to a higher value of f_c in this direction.

2.2.2 Optical site-selective spectroscopy. Absorption and optical site-selective fluorescence spectroscopy allow the determination of the energetic structure of the erbium ion in $LiNbO_3$. Details of this investigation are given in [44]. As the investigation of diffusion doped materials needs special instrumentation, Er^{3+} doped bulk crystals were studied although it is still an open question if these exhibit identical spectroscopic properties.

To obtain information on the energy levels of Er^{3+} in $LiNbO_3$, optical absorption spectra of different transitions

Table 3. Coherent positions, $\Phi_c^{(hkl)}$, and coherent fractions, $f_c^{(hkl)}$, extracted from the XSW-measurements. The coherent positions are given in units of the diffraction plane spacings with $\Phi_c^{(hkl)} = 0$ being located on planes containing Nb atoms

Reflection	Φ_{Er}	f_{Er}	Φ_{Nb}	f_{Nb}
$(1\bar{1}0\bar{4})$	0.98 ± 0.03	0.86 ± 0.02	0.99 ± 0.03	0.85 ± 0.03
$(000\bar{6})$	0.535 ± 0.03	0.62 ± 0.03	0.95 ± 0.05	0.60 ± 0.04

◀

Fig. 7a–d. Er:$LiNbO_3$ surface morphology depending on the degree of the depletion of the diffusion reservoir. **a–c** The diffusion reservoir is not completely exhausted. The remaining Er_xNb_y-oxide form islands. A non uniform surface coverage can be observed. **d** Er:$LiNbO_3$ surface morphology immediately after the depletion of the diffusion reservoir at $t \approx t_1$. If the diffusion reservoir is completely exhausted the surface is comparable to an untreated substrate surface. (Samples: $d_{Er} = 12.2$ nm, $t_{diff} = 30$ h, T_{diff}: **a** 1060 °C, **b** 1100 °C, **c** 1130 °C and **d** $d_{Er} = 11.3$ nm, $t_{diff} = 30$ h, $T_{diff} = 1130$ °C, respectively)
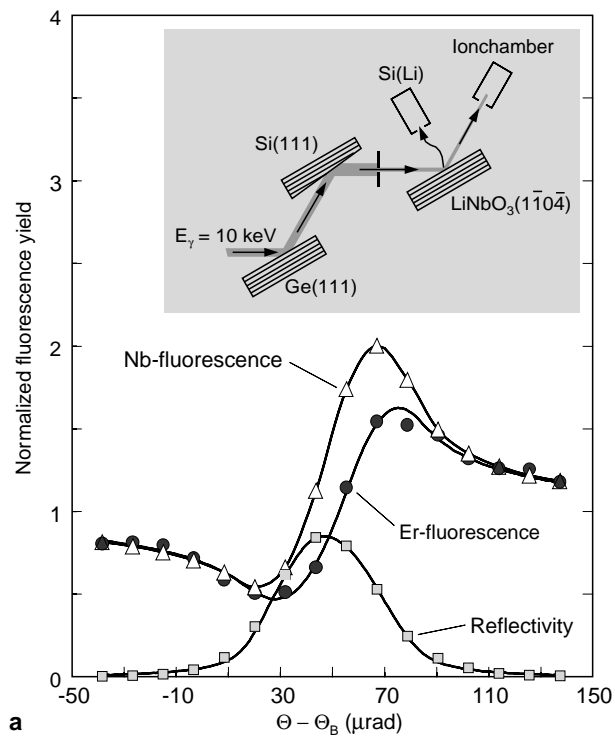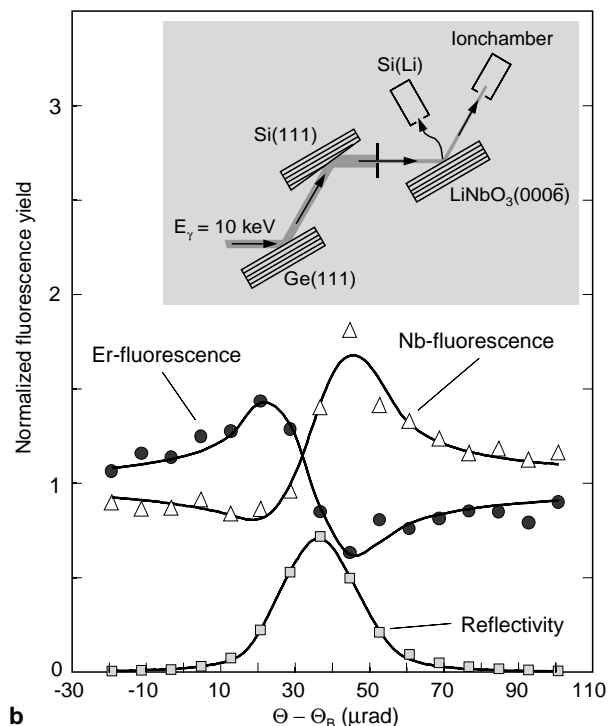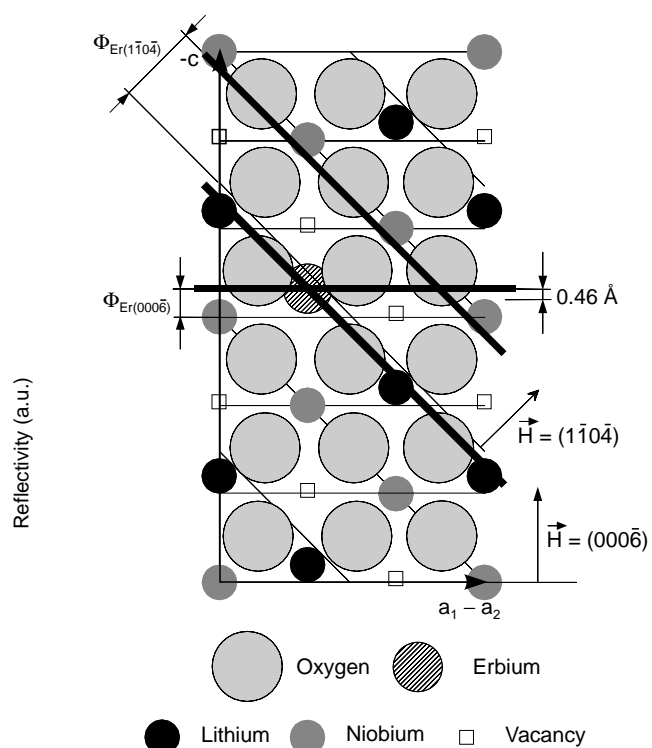
Fig. 8a, b. Normalised XSW-data for the reflectivity, Nb- and Er-fluorescence yields with associated theoretical fits (△ Nb-fluorescence, ○ Er-fluorescence, □ rocking curve). **a** measurements along the $(1\bar{1}0\bar{4})$ direction, **b** measurements along the $(000\bar{6})$ direction (The experimental setups and the combination of the monochromator and sample crystals are shown in the insets.)


Fig. 9. Diagonal cut through the hexagonal unit cell. The two slanted black bands mark the measured coherent position $\Phi_{Er}^{(hkl)}$ of erbium atoms with respect to the $(1\bar{1}0\bar{4})$ planes, the horizontal black band the position with respect to the $(000\bar{6})$ planes indicated by thin lines. The point of intersection of these bands at a sixfold co-ordinated lattice site mark the valid erbium position ($\vec{H}$ indicates the diffraction vector of the corresponding diffraction planes)

from the $^4I_{15/2}$ ground state to upper energy levels up to the $^4G_{11/2}$ were recorded. The measurements reported here will only consider the transitions involving the $^4F_{9/2}$ excited state as an example.

Figure 10 presents the σ- and π-polarised absorption spectra of the $^4I_{15/2} \Rightarrow {}^4F_{9/2}$ transition. The spectral resolution was better than 0.3 meV. As the spectra were taken at $T = 5$ K only the lowest sublevel of the $^4I_{15/2}$ ground state is populated so that the observed number of lines directly images the splitting of the excited state. The sublevels are marked as S_i with $i = 1 \dots (J + 1/2)$. The fivefold splitting of the $^4F_{9/2}$ as well as the observed polarisation states of the sublevels are consistent with the crystal field theory and with the selection rules for electric and magnetic dipole transitions. The observed splitting confirms the C_3 point symmetry of the Er^{3+} site as determined by the XSW-measurements.

In several of the investigated spectra an additional substructure of the lines was observed. In Fig. 10 all transitions are split into two components (labelled by an extra index 1 and 2 in the figure). This substructure is due to splitting into individual components. The double structure was observed for all transitions investigated in the 1.8–3.3 eV range. Additionally, the $^4I_{15/2} \Rightarrow {}^2H_{11/2}$ and the $^4I_{15/2} \Rightarrow {}^4G_{11/2}$ transitions showed a clear fourfold structure due to further slight perturbations of the local symmetry of the crystal field [44]. This further splitting can also be observed in the $^4F_{9/2}$ absorption spectra as shoulder or distortion of the lineshape (indicated by arrows in Fig. 10b). The maximum fourfold structure implies the existence of at least four Er^{3+}
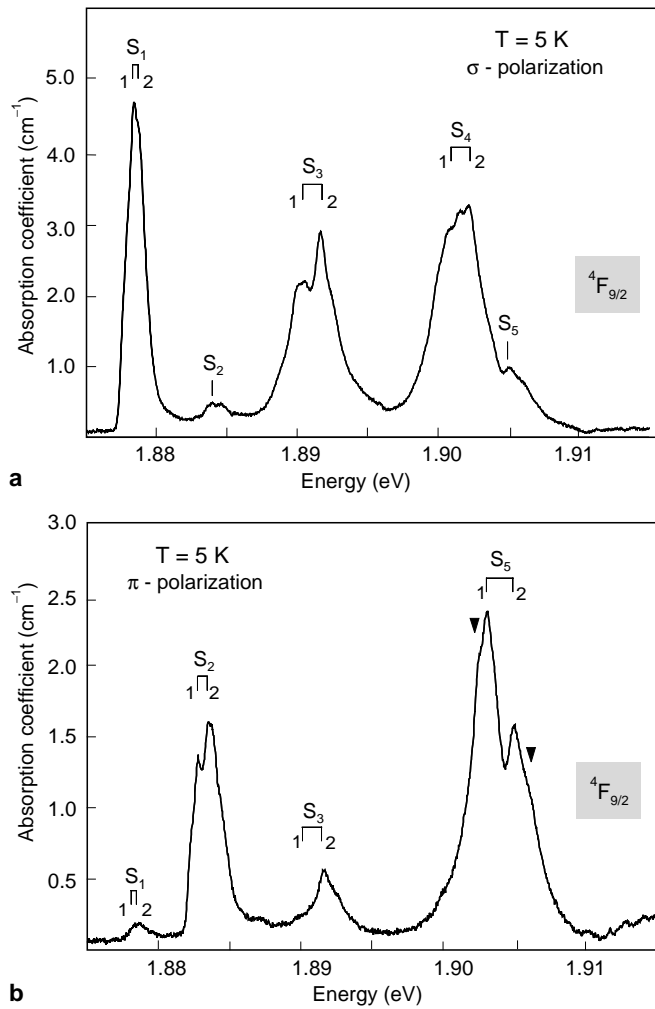
Fig. 10. Absorption spectra for Er^{3+} in $LiNbO_3$ **a** for σ-polarisation and **b** for π-polarisation of the $^4I_{15/2} \Rightarrow {}^4F_{9/2}$ transition at 5 K showing the (J + 1/2)-splitting ($S_1 \dots S_5$). An additional structure within the sublevels was also observed due to different local crystal field environments of the Er_{Li}. (1 and 2 mark the Er_1- and Er_2-centres; the arrows in **b** indicate two further sites different from those labelled above.)

sites with C_3 symmetry characterised by different local environments.

As shown by the XSW results erbium is located close to the lithium site, Er_{Li}. Therefore, a significant occupation of the Er_{Nb} site as well as the structural vacancy site, $Er_\square$, can be excluded as reason for the observed splitting in the absorption spectra. The spectroscopically observed different lattice sites are caused by different local symmetries of the crystal field acting on the Er^{3+} on nearly equal geometric lattice sites. We assume that this is due to locally different arrangements of charge compensating defects. The defect arrangement can both influence the local field at the Er^{3+} site and cause a slight shift of the erbium ion relative to the neighbouring oxygen triangle as discussed by *Garcia-Solel* [45] resulting in a different local field as well. This conclusion is supported by the XSW-results suggesting a distribution function of erbium extended along the *c*-direction. It
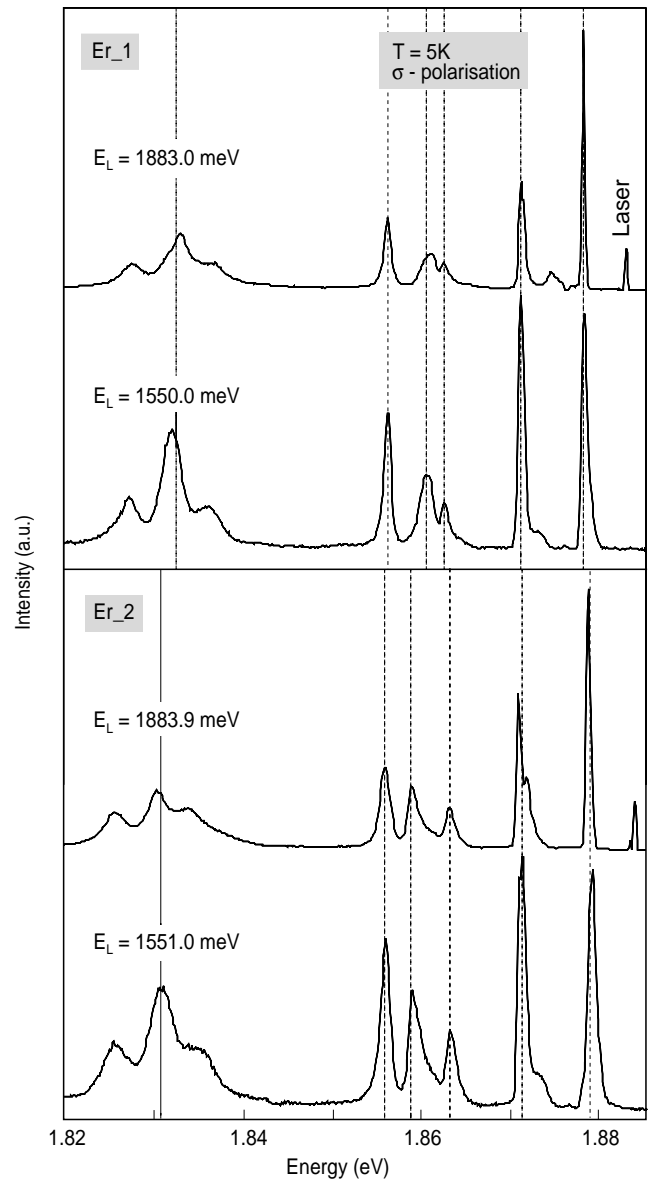
Fig. 11. Site-selectively excited σ-polarised $^4F_{9/2} \Rightarrow {}^4I_{15/2}$ emission spectra of Er^{3+} in $LiNbO_3$ at 5 K. The spectra generated at 1.88 eV are resonantly excited. The other two are generated upon infrared excitation at 1.55 eV by upconversion via excited state absorption

seems to be more convenient to call these sites erbium centres.

Using site-selective excitation it was possible to analyse two of the four different components of the sublevels in detail and to determine the difference of the Stark splitting for the $^4I_{15/2}$ ground state. The two erbium centres belonging to these components are labelled as Er_1 and Er_2.

Figure 11 shows the σ-polarised $^4F_{9/2} \Rightarrow {}^2I_{15/2}$ emission spectra of $Er:LiNbO_3$ which were site selectively excited. The upper two spectra correspond to the Er_1 centre resonantly and non-resonantly excited at 1.8830 eV and 1.550 eV, respectively, while the lower two spectra belong to Er_2 excited at 1.8839 eV and 1.551 eV, respectively. The spectra excited at about 1.55 eV involved the
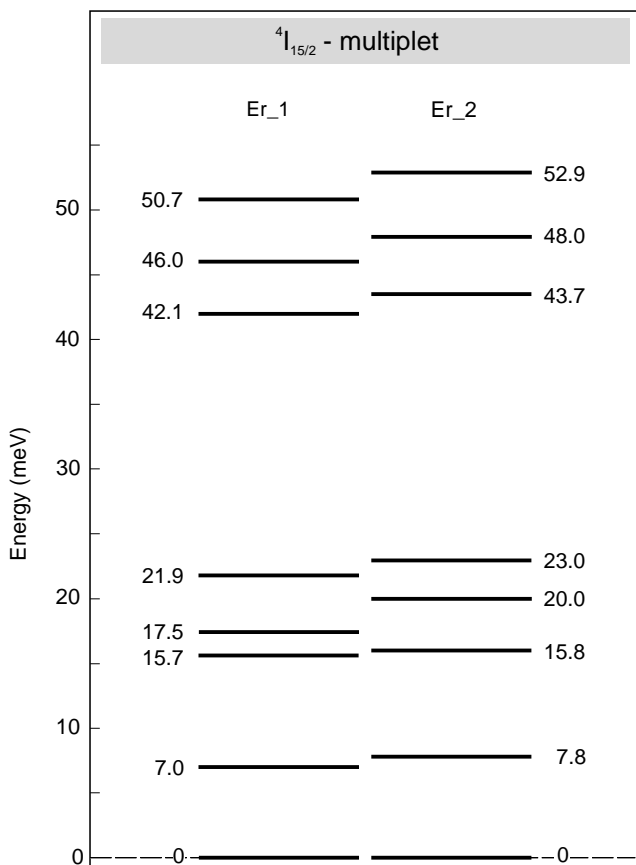
Fig. 12. Energy level diagram of the $^4I_{15/2}$ ground state of the two investigated slightly different lattice sites of erbium in LiNbO$_3$ (erbium centres Er_1 and Er_2) derived from luminescence spectra

$^2H_{11/2}$ state and are generated by upconversion upon excitation in the infrared.

The observed eight emission lines are due to transitions from the lowest $^4F_{9/2}$ sublevel into the eight-fold split $^4I_{15/2}$ ground state. The differences in energetic positions of the lines reflect the different ground state splitting for the two Er^{3+} sites. The non-resonant excitation involving upconversion and relaxation processes demonstrates that for a given erbium centre the appearance of the spectra is independent of the excitation mechanism.

From analysing the spectra it is straightforward to derive the ground state level diagrams of the Er_1 and Er_2 centres as shown in Fig. 12. Several nonequivalent Er^{3+} sites were found in LiNbO$_3$ before (see e.g. [46, 47]), however, a detailed comparison of energy states is difficult due to different spectral resolution and sample temperatures.

3 Model of erbium incorporation

Considering the point defect structure of congruent LiNbO$_3$ the incorporation of erbium will be discussed. The point defect structure of congruent LiNbO$_3$ can be described by two models: The Nb-vacancy model [48]

$$[Li_{1-5x}Nb_{5x}][Nb_{1-4x}\square_{4x}]O_3 \tag{12}$$
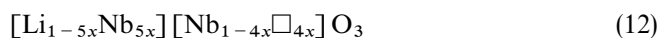
and the Li-vacancy model confirmed by recent investigations [4, 5]

$$[Li_{1-5x}Nb_x\square_{4x}]NbO_3, \tag{13}$$

where $\square$ marks a vacant cation lattice site. In both cases the oxygen sublattice is completely occupied. The difference in both models is the creation of charge compensating vacancies due to niobium occupation of lithium sites. The fact that most of the dopants incorporated into LiNbO$_3$ occupy lithium sites is a strong hint for the validity of the Li-vacancy model. Due to the strong covalent bonding within the NbO$_6$-octahedra it is an elementary constituent of the LiNbO$_3$ structure even existing as fundamental local structure in the melt [49]. The structure of LiNbO$_3$ can be characterised by Nb-filled oxygen octahedras forming a corner-linked framework.

Theoretical simulations of the LiNbO$_3$ defect structure had shown that the formation of Nb-vacancies is energetically unfavourable, as the formation energy of a Li-Frenkel defect is low. From the energetic point of view the formation of antisite complex defects, $(Nb_{Li}\square_{Nb})'$, due to site swapping is probable [50]. This kind of defect can be considered as connecting element between the two defect models mentioned above. Its formation is discussed as function of temperature [36]. But at high temperatures the antisite defect should not be the predominant kind of defect.

For the erbium incorporation it is suggested that due to the counterdiffusion of both niobium and lithium to the surface layer and especially due to the lithium outdiffusion Li-vacancies are created. These are occupied by indiffusing erbium and are needed for local charge compensation due to the incorporation of ions of higher charge than the lithium ion, respectively. The incorporating mechanism can be written formally as

$$Li_{Li} + Nb_{Li}^{\cdots\cdot} + 4\square_{Li} + 2\,Er^{3+} \Rightarrow 2Er_{Li}^{\cdots}$$

$$+ 4\square_{Li'} + Li^+ + Nb^{5+}$$
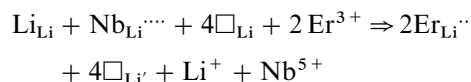
No remarkable change of the point defect structure seems to be necessary. At the surface LiNbO$_3$ is formed growing on the top of the substrate. It can be assumed that diffusion will occur through the easiest path via vacant cation sites and the structural octahedral vacancies.

4 Conclusions

The diffusion of erbium into LiNbO$_3$ can be described by Fick's laws of diffusion with a concentration-independent diffusion coefficient and a temperature-dependent maximum solubility of erbium in LiNbO$_3$. Corresponding to the crystal structure of LiNbO$_3$ the diffusion coefficient shows an anisotropy described by a second rank tensor. It is about two orders of magnitude smaller than that of titanium. The solubility of erbium is about one order of magnitude smaller than that of titanium [6]; it grows exponentially with rising temperature. As long as the diffusion reservoir is not exhausted the surface of the substrate is rough due to island formation of an Er$_x$Nb$_y$-oxide which forms the diffusion reservoir at high

temperatures. The diffusion data determined by our experiments enable complete phenomenological modelling of the diffusion of erbium into $LiNbO_3$.

Erbium is incorporated into $LiNbO_3$ on a vacant Li-site or replaces lithium. The exact position of erbium compared with the lithium site is shifted by 0.46 Å in (-c)-direction. Absorption measurements and site-selective spectroscopy found four slightly different, but well defined erbium sites. This seems to be caused by perturbations of the local crystal field due to small local variations in the arrangement of charge compensating defects.

References

1. H.M. O'Bryan, P.K. Gallagher, C.D. Brandle: J. Am. Ceram. Soc. **68/9** (1985) 493–496
2. P.F. Bordui, R.G. Norwood, C.D. Bird, G.D. Galvert: J. Crystal Growth **113**, (1991) 61–68
3. I.Baumann, P. Rudolph, D. Krabe, R. Schalge: J. Crystal Growth **128**, (1993) 903–908
4. N. Zotov, H. Boysen, F. Frey, T. Metzgers, E. Born: J. Phys. Chem. Solids **55/2**, (1994) 145–152
5. N. Iyi, K. Kitamura, F. Izumi, J.K. Yamamoto, T. Hayashi, H. Asano, S. Kimura: J. Solid State Chem. **101**, (1992) 340
6. B. Guenais, M. Baudet, M. Minier, M. Le Cun: Mat. Res. Bull. **16**, (1981) 643–653
7. H. Takei, T. Katsumata: Mat. Res. Bull. **17**, (1982) 111–116
8. B.C. Grabmaier, F. Otto: J. Crystal Growth **79**, (1986) 682–688
9. A. Kling, D. Kollewe, B.C. Grabmaier: Nucl. Instr. Methods Phys. Res. **B64/1–4**, (1992) 232–236
10. I. Baumann, R. Brinkmann, Ch. Buchal. M. Dinand, M. Fleuster, H. Holzbrecher, W. Sohler, H. Suche: Proc. 6th Europ. Conf. on Integrated Optics (ECIO'93), Neuchâtel, 3–14
11. E. Lallier, J.P. Pocholle, M. Papuchon, Q. He, M. deMicheli, B. Ostrowsky: Electronics Lett. **27/11**, (1991) 936–937
12. M. Hempstead, J.S. Wilkinson, L. Reekie: IEEE Photon. Technol. Lett. **4/8**, (1992) 852–854
13. R. Brinkmann, W. Sohler, H. Suche, C. Wersig: IEEE J. Quant. Electron. **28/2**, (1992) 466–470
14. J.K. Jones, J.P. deSandro, M. Hempstead, D.P. Shepherd, A.C. Large, A.C. Tropper, J.S. Wilkinson: to be published in Optics Lett.
15. J.P. deSandro, J.K. Jones, D.P. Shepherd, J. Webjörn, M. Hempstead, J. Wang, A.C. Tropper: Proc. 7th Europ. Conf. on Int. Opt. (ECIO'95), Delft, post-deadline papers 17–20
16. R. Brinkmann, I. Baumann, M. Dinand, W. Sohler, H. Suche: IEEE J. Quantum Electronics **30/10**, (1994) 2356–2360
17. I. Baumann, R. Brinkmann, M. Dinand, W. Sohler, S. Westenhöfer: IEEE J. Quantum Electron. **3219** (1996) 1695–1706
18. H. Suche, I. Baumann, D. Hiller, and W. Sohler, Electronics Lett. **29/12**, (1993) 1111–1112
19. I. Baumann, D. Johlen, H. Suche, F. Tian: Proc. 20th Europ. Conf. on Opt. Com. (ECOC'94), Firenze, **4** (post deadline paper) 99–102
20. J. Söchtig, R. Groß, I. Baumann, W. Sohler, H. Schütz, R. Widmer: Electronics Lett. **31/7**, (1995) 551–552
21. R. Brinkmann, M. Dinand, I. Baumann, Ch. Leifeld, W. Sohler, H. Suche: IEEE Photonics Technol. Lett. **6/4**, (1994) 519–521
22. H. Suche, D. Hiller, I. Baumann, W. Sohler: IEEE Photon. Techn. Lett. **7/5**, (1995) 505–507
23. M. Fleuster, Ch. Buchal, H. Holzbrecher, U. Breuer, M. Dinand, H. Suche, R. Brinkmann, W. Sohler: Mat. Res. Soc. Symp. Proc. **279**, (1993) 279
24. S. Bauer, L. Beckers, M. Fleuster, J. Schubert, W. Zander, Ch. Buchal: Mat. Res. Soc. Symp. Proc. **341**, (1994) 283
25. V.T. Gabrielyan, A.A. Kaminskii, L. Li: Phys. Stat. Sol. (a) **3** (1970) K37–K42
26. R.J. Esdaile: J. Appl. Phys. **58/2**, (1985) 1070–1071
27. H. Oechner: Thin film and Depth Profile Analysis, ed. by H. Oechner, Springer-Verlag Heidelberg 1984
28. A. Wucher, Fresenius J: Anal. Chem. **346**, (1993) 3–10
29. H. Oechsner: Appl. Surface Sci. **70/71**, (1993) 250–260
30. W. Bock, M. Kopnarski, H. Oechsner, Fresenius J: Anal. Chem. **353**, (1995) 510–513
31. R. Jede, H. Peters, G. Dünnebier, O. Ganschow, U. Kaiser, K. Seifert: J. Vac. Sci. Technol. **A6/4**, (1988) 2271–2279
32. W.K. Chu, J.W. Mayer, M.A. Nicolet: "Backscattering Spectroscopy" (Academic Press, New York 1978)
33. Th. Gog, M. Griebenow, G. Materlik: Phys. Lett. A **181**, (1993) 417–420
34. Th. Gog, T. Harasimowicz, B.N. Dev, G. Materlik: Europhys. Lett. **25/4**, (1994) 253–258
35. Th. Gog, G. Materlik: "X-ray Standing Wave Determination of Crystal Lattice Positions of Impurities in Ferroelectric Lithium Niobate" in F. Agullo-Lopez (ed.) "Insulating Materials for Optoelectronics", World Scientific Publishing (1995)
36. D.P. Birnie III: J. of Mat. Sci. **28**, (1993) 302–315
37. J. Crank: The Mathematics of Diffusion, Clarendon Press, Oxford 1975
38. M. Dinand: PhD thesis, University of Paderborn 1995
39. A.H. Cottrell: "Theoretical structural metallurgy" (Arnold V, London 1954)
40. M. Fleuster: PhD thesis, Forschungszentrum Jülich 1994
41. M.N. Armenise, C. Canali, M. DeSario, A. Carnerea, P. Mazzoldi, G. Celotti: J. Appl. Phys. **54/11**, (1983) 6223–6231
42. C.E. Rice, R.J. Holmes: J. Appl. Phys. **60/11**, (1986) 3836–3839
43. S.C. Abrahams, J.M. Reddy, J.L. Bernstein: J. Phys. Chem. Solids **27**, (1966) 997–1012
44. O. Witte, H. Stolz, W. von der Osten: J. Phys. D: Appl. Phys. **29** (1996) 561–568
45. J. Garcia-Solel: "Non Equivalent Active Centres and their Lattice Location in $LiNbO_3$ Minilasers" Workshop on "Rare Earth Doped Optical Waveguides", Les Houches, France, June 1994, p. 71–94
46. R. Duchowicz, L. Nunez, J.O. Tocho, F. Cusso: Solid State Com. **88/6**, (1993) 439–442
47. D.M. Gill, J.C. Wright, L. McCaughan: Appl. Phys. Lett. **64**, (1994) 2489–2491
48. S.C. Abrahams, P. Marsh: Acta Cryst. **B42**, (1986) 61–68
49. K. Sugiyama, K. Nomura, Y. Waseda, P. Andonov, S, Kimura, K. Shigematsu: Z. Naturforsch. **45a** (1990) 1325–1327
50. H.J. Donnerberg, S.M. Tomilson, C.R.A. Catlow: J. Phys. Chem. Solids **52/1**, (1991) 201–210